Article

Nuclear Power Plant Prestressed Concrete Containment Vessel Structure Monitoring during Integrated Leakage Rate Testing Using Fiber Bragg Grating Sensors

Jinke Li [1], Kaixing Liao [2], Xianglong Kong [2], Shengyuan Li [1], Xinwang Zhang [1], Xuefeng Zhao [1,*] and Changsen Sun [3]

[1] State Key Laboratory of Coastal and Offshore Engineering, School of Civil Engineering, Dalian University of Technology, Dalian 116024, China; jinkeli@mail.dlut.edu.cn (J.L.); lishengyuan@mail.dlut.edu.cn (S.L.); zhangxinwang@mail.dlut.edu.cn (X.Z.)

[2] Ageing Management Department, Suzhou Nuclear Power Research Institute Co., Ltd., Suzhou 215004, China; liaokaixing@cgnpc.com.cn (K.L.); kongxianglong@cgnpc.com.cn (X.K.)

[3] School of Physics and Optoelectronic Engineering, Dalian University of Technology, Dalian 116024, China; suncs@dlut.edu.cn

* Correspondence: zhaoxf@dlut.edu.cn; Tel.: +86-411-8470-6261

Abstract: As the last barrier of nuclear reactor, prestressed concrete containment vessels (PCCVs) play an important role in nuclear power plants (NPPs). To test the mechanical property of PCCV during the integrated leakage rate testing (ILRT), a fiber Bragg grating (FBG) sensor was used to monitor concrete strain. In addition, a finite element method (FEM) model was built to simulate the progress of the ILRT. The results showed that the strain monitored by FBG had the same trend compared to the inner pressure variation. The calculation results showed a similar trend compared with the monitoring results and provided much information about the locations in which the strain sensors should be installed. Therefore, it is confirmed that FBG sensors and FEM simulation are very useful in PCCV structure monitoring.

Keywords: prestressed concrete containment vessel (PCCV); fiber Bragg grating (FBG); integrated leakage rate test (ILRT); finite element method (FEM); structure health monitoring (SHM)

1. Introduction

The prestressed concrete containment vessel (PCCV) of the nuclear power plant (NPP) is the last barrier of the nuclear reactor. The PCCV is so important that many sensors were installed during construction to monitor different physical quantities. For example, vibrating wire strain gauges were used to monitor the concrete structure strain, invar wires were used to monitor vertical deflection, and so on. After the construction of the PCCV, there were few cracks (2 visible cracks in total at the height of +22 m in this paper) in the concrete. To verify the construction quality, mechanical properties and airtightness of the PCCV, the integrated leakage rate testing (ILRT) was implemented with a certain time interval. After the ILRT, new cracks appeared due to the increasing pressure inside the PCCV. After the second ILRT at another PCCV, there were about 20 cracks at the same location. Some of them may lead to air leakage due to the increasing inner pressure, so concrete strain monitoring is very important. As a consequence, it would be very useful to monitor PCCV deformation during the ILRT.

In the construction of the PCCV, about 20 to 60 vibrating wire strain gauges were embedded in concrete to monitor strain. At the same time, the thermocouples were also embedded to monitor the

temperature change for temperature compensation. However, once the embedded strain sensors are damaged, there should be a method to compensate.

Nowadays, fiber optic sensors are widely used in the civil engineering structure health monitoring (SHM). Glišić and Simon [1] used the stiff Surveillance d'Ouvrage par Fibers Optics (SOFO) sensor to monitor the concrete deformation at a very early concrete age. The results showed that the SOFO sensor can monitor concrete deformation. SOFO was also used for concrete strain measurement system in monitoring the 1:4 scale model of the PCCV built by Sandia National Laboratories [2]. Zhao et al. [3] used white light interferometer (WLI) method to monitor the rebar expansion by coiling the fiber optic on the rebar's surface. Apart from these, Brillouin optical time domain analysis (BOTDA) was widely used in the tunnel, bridge, pipelines and so on. Inaudi and Glišić [4] used Brillouin and Raman scattering to detect leakage in the brine and gas pipelines. They identified the leakage position successfully. In order to verify whether fiber Bragg grating (FBG) could be used in the NPP structure, Ferdinand et al. [5] did a series of experiments. Fortunately, FBG showed good resistance to γ-ray irradiations. This meant FBG could be used in the PCCV structure even in conditions where FBG received nuclear radiation. In order to monitor the prestress force of prestress tendon, Jang et al. [6] installed FBG on the PCCV cylindrical wall during the ILRT. The results showed that the vertical strain was 17–25 με and the hoop strain was about 54–90 με. Besides, the impact signal analysis technique was used in evaluating the prestress force of bonded tendons and showed good potential. Moreover, FBG was widely used in other fields. Leng and Asundi [7] used FBG to monitor the cure progress of carbon fiber reinforced plastic (CFRP) composite materials and detected the occurred damage successfully. Wan et al. [8] adopted long-gauge FBG sensors to monitor the strain and deflection of a prestressed box bridge. The FBG monitoring data was used to detect damage of the bridge. Perry et al. [9] welded FBG on the strand to measure the prestress force. This weld fabrication allowed the instrumented strand to measure the stress up to 1300 MPa. Li et al. [10] used an active thermal probe to detect steel reinforcement corrosion. Due to the poor thermal conductivity of corrosion products, they used carbon fiber strands to generate heat and FBG temperature sensors to monitor the temperature change. The results suggested that there was a correlation between corrosion severity and temperature response.

Since fiber optic sensors exhibit numerous advantages such as superior durability, high sensitivity, electromagnetic interference immunity and γ-ray irradiation immunity, using them in PCCV monitoring is a good choice. When the embedded vibrating wire strain gauges are damaged, the fiber optic sensors can compensate. In this paper, FBG was proven to be able to monitor the strain development of PCCV cylindrical wall.

Except for the engineering application, researchers used finite element method (FEM) model to simulate the PCCV and analyzed the failure model. As PCCV was designed to withstand certain inner pressure even in the case of a loss of coolant accident (LOCA), Hu and Lin [11] used the FEM model with a nonlinearity constitutive model to predict the ultimate pressure capacity and failure mode. The results found that the ultimate pressure capacity of the PCCV was 0.886 MPa, which was 86% higher than the design pressure. Cracks were likely to occur near the apex of the dome, the junction of the dome and cylinder and the bottom of the cylinder. Sang et al. [12] used an axisymmetric model and a 3D model to simulate 1:4 scale model of the PCCV. Both high temperature loading and internal pressure were considered in the analysis. The analysis results indicated the temperature affected the behavior of liner plate, but had little impact on the ultimate pressure capacity of the PCCV. Lee [13] used a degenerated shell element in FEM model for ultimate pressure capacity evaluation. For precise simulation, this FEM model involved many material properties including a tension stiffening model, shear transfer mechanism, crack occurrence criteria and so on. The results showed the initial crack occurred at the internal pressure 0.83 MPa. In contrast to paper [11], the crack began in the middle part of the wall and then spread to the upper part of the wall at pressure 1.14 MPa. Other than the whole PCCV FEM model, the simplified model was also used. Bílý and Kohoutková [14] used part of the cylindrical wall of PCCV for sensitivity analysis. The sensitivity analysis of seven types of geometry

and five kinds of load step was conducted. Results showed that the steel liner and temperature effect were the most important factors. Jones et al. [15] compared the bonded PCCV with unbonded PCCV in FEM modeling and predicted the failure at the extreme inner pressure. The results indicated that the cylinder wall deformations were larger with bonded tendons and so were the peak strains during the internal pressurization. Shokoohfar and Rahai [16] adopted a nonlinear FEM model to analyze the thermal and mechanical behaviors of the PCCV that was subjected to temperature loading and internal pressure. The analysis showed that the temperature had little impact on the ultimate pressure capacity of the PCCV.

In this paper, we adopted FBG to monitor the PCCV during the ILRT. Moreover, the FEM model was built to simulate the pressurization and depressurization process. Firstly, the monitoring results were compared to the variation trend of pressure platform. Secondly, the rationality of the monitoring results was discussed because of abrupt temperature drop. Thirdly, the FEM model calculation results were compared with the monitoring results to testify the FEM model. Last, the calculation results were analyzed for sensor placement.

2. The Experimental Process and the FEM Model

2.1. Basic Principle of FBG

The FBG working principle was explained in the paper [17,18]. If FBG and the host material were bonded perfectly, the strain of host material would be transferred to FBG. Then the wavelength shift of FBG ($\Delta\lambda_b$) would be influenced by the load induced strain (ε_1). The temperature change (ΔT). $\Delta\lambda_b$ is given by Equation (1).

$$\frac{\Delta\lambda_b}{\lambda_b} = (1 - p_e)\varepsilon_1 + (1 - p_e)\alpha_h\Delta T + \xi\Delta T \tag{1}$$

The parameter p_e is the optical fiber photo-elastic coefficient, α_h is the thermal expansion coefficients of the host material and ξ is the thermo-optic coefficient [18]. From Equation (1), it is clear that the stain measured by FBG will depend on the strain of host material, the thermal expansion of host material and the temperature influence on index of refraction of the fiber optic sensor. Since concrete is a composite material, α_h varies at different locations. To simplify the calculation, thermal expansion of concrete was not considered in strain calculation. In order to separate fiber optic expansion caused by temperature from the monitoring strain, the temperature compensating method [19] was used. The temperature-compensating FBG (FBG-T-01, manufactured and calibrated by NingBo ShanGong Intelligent Security Technology, Co., Ltd., Ningbo, China) and strain FBG (SQ-FBG-GS01, manufactured and calibrated by NingBo ShanGong Intelligent Security Technology, Co., Ltd.) were calibrated in the laboratory before installing them in-site.

2.2. FBG Sensors Deployment

During the in-site monitoring, FBG sensors were installed on PCCV cylindrical wall at an NPP in China. The top elevation of the auxiliary structure is 22 m as shown in Figure 1b. Apparently, the roof of auxiliary structure provided large space for installing FBG. As a result, the monitoring location was chosen at the mid height of the PCCV (see Figure 1a).

On the cylindrical wall of PCCV, two kinds of FBG were installed as shown in Figure 2. The Figure 2a shows the general measuring point which consists of a vertical direction strain FBG and a circumferential direction strain FBG. In total, there were four general measuring points around the PCCV. Besides, Figure 2b shows the crack measuring point which consists of two circumferential FBG sensors which are perpendicular to the concrete crack. During installation, these two strain FBG sensors were pasted across the concrete crack. Both general measuring points and crack measuring points had a temperature-compensating FBG beside the strain FBG.

Before installation, FBGs were divided into six groups and fusion spliced together. Here were the processes of the installation. Firstly, the concrete surface was polished to clear the dust away.

Secondly, the FBGs were pasted on the cylindrical wall by using No. 502 glue for primary fixing. Thirdly, epoxy resin was smeared on FBGs for reinforcement and protection. After those processes, the optic fiber connecting line was pasted on concrete surface. At last, a fiber optic connecting line was connected to Optical Sensing Interrogator sm125 (manufactured by MICRON OPTICS) for data collection. In order to distinguish those FBG in one channel, the wavelength of each FBG and the specific location was recorded after installation.

The measuring points are located at the middle of the PCCV as shown in Figure 3. The specific locations of each FBG are summarized in Figure 3.
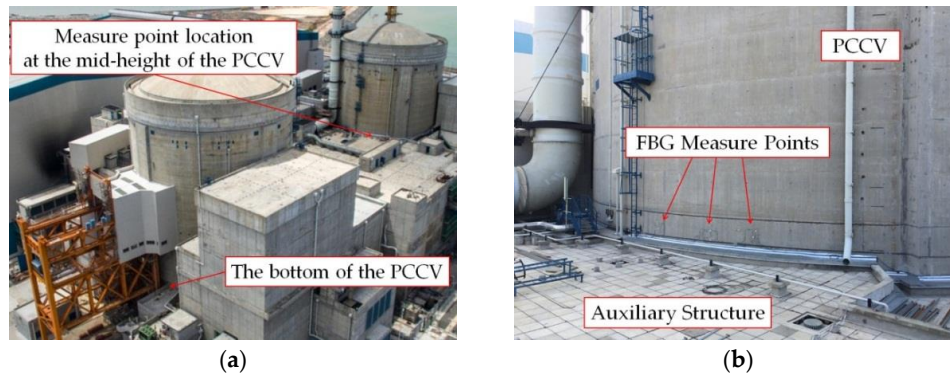
Figure 1. The location of fiber Bragg grating (FBG) measuring points on the prestressed concrete containment vessel (PCCV). (**a**) Prospect of the measuring points; (**b**) Close shot of the measuring points.
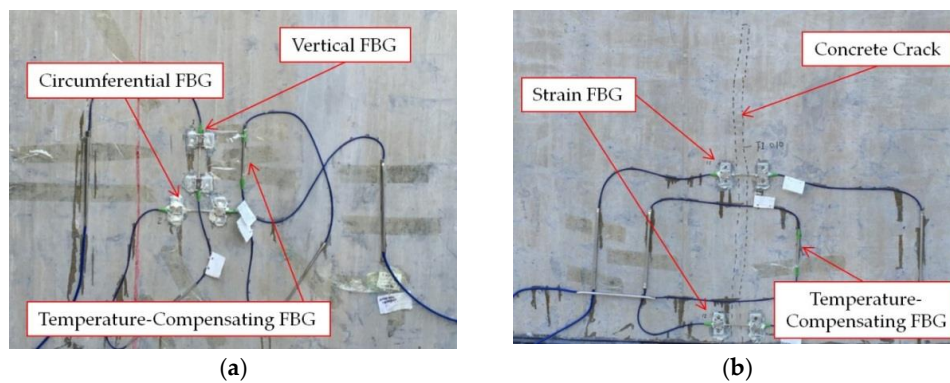
Figure 2. Two types FBG measuring points. (**a**) General measuring point; (**b**) Crack measuring point.
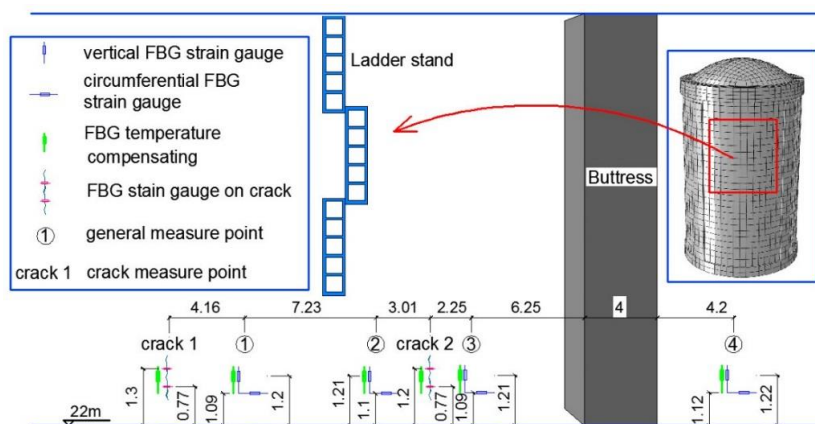
Figure 3. The measuring point locations on the PCCV and the specific location of each measure point (length unit: m).

2.3. The Pressure Time Table

Due to the importance of the PCCV, the concrete structure must be sufficiently confined and leak-tight both in service life and even in the event of LOCA. To test the mechanical property and the leakage rate of the PCCV, ILRT was carried out. ILRT should be conducted every 10 years. During the ILRT, the pressure inside the containment vessel will increase and decrease according to a certain plan. And the ILRT pressure time table is shown in Figure 4.
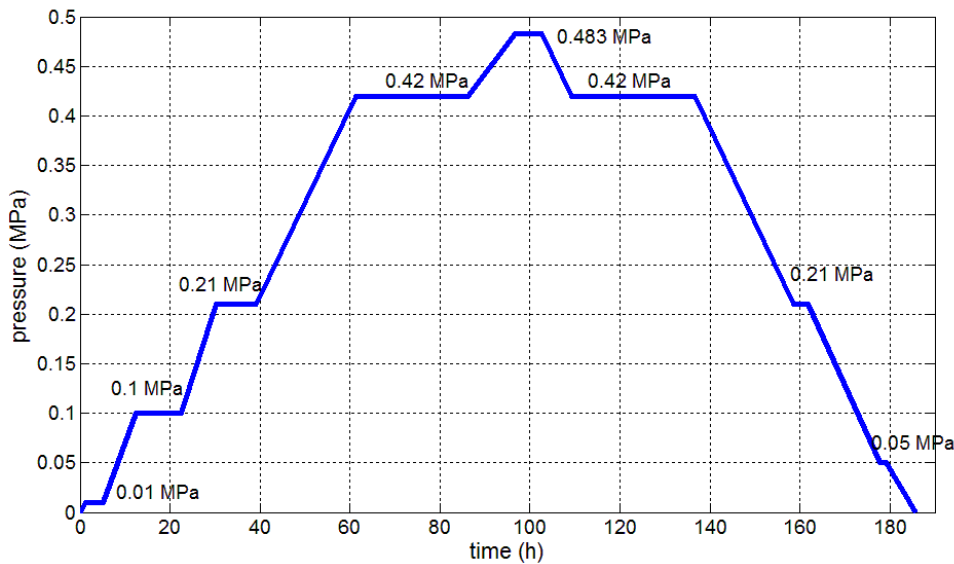
Figure 4. The pressure time table.

In Figure 4, there are several pressure platforms such as 0.21, 0.42, 0.483 MPa and so on. These pressure platforms lasted for several hours for engineers to measure the leakage rate and find the structure defects. The design pressure of the PCCV is $P_d = 0.42$ MPa and the ultimate pressure is $1.15\,P_d = 0.483$ MPa. After the ILRT, the pressure reduced to 0 MPa. In-site, FBGs were installed three days before ILRT and data was collected 12 h before ILRT.

2.4. The FEM Model

2.4.1. Hypothesis

Assuming that the surface strain of PCCV was a constant value after construction, which means the temperature influence, the prestress loss of prestress tendon, the shrinkage and creep of concrete and other factors did not cause strain on the surface of the cylindrical wall. Then, the pressurization and depressurization process inside the PCCV was simulated. Because there was no cavity like the equipment hatch at the measuring points' side on the cylindrical wall, the cavity on concrete wall was not modeled for simplification.

2.4.2. Geometry

Prior to FEM modelling, the 3D geometric model was built. The cross section of the PCCV is shown in Figure 5a and the layout of the prestress tendons in cylindrical wall is shown in Figure 5b. As shown in Figure 5b, the thickness of cylindrical wall is 0.9 m, and thickness of anchorage block is 1.5 m. The steel liner is a 6-mm thick steel plate on the inner surface of the cylindrical wall.
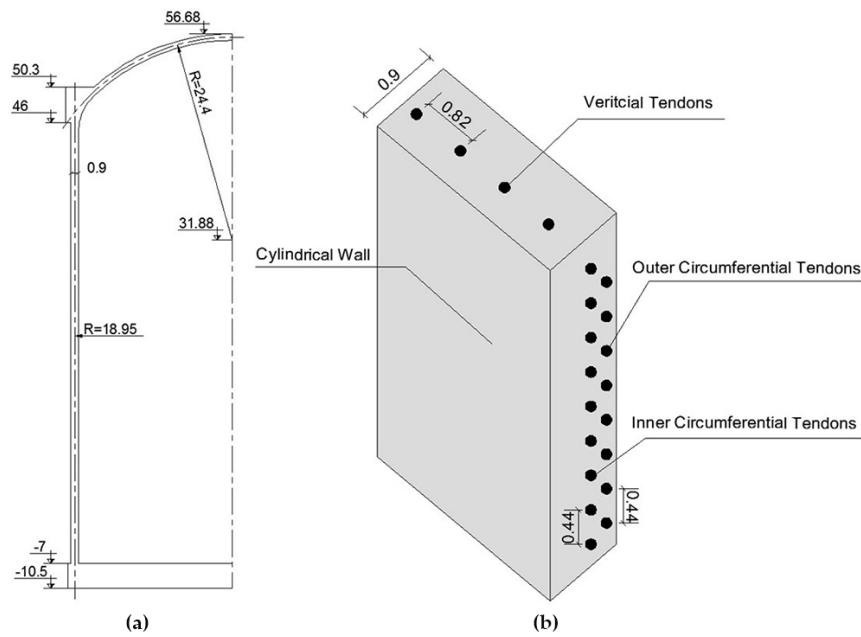
Figure 5. The geometric dimension of PCCV. (**a**) The cross section of PCCV (length unit: m); (**b**) Layout of prestress tendons in cylindrical wall (length unit: m).

2.4.3. Material

In previous research, the results of [11] showed material nonlinearity would have an effect on the displacement of the PCCV when the internal pressure was beyond 0.886 MPa. According to the results in [15], the radial displacement, the tendon strain and concrete strain changed a little from the pressure 0 MPa to 0.585 MPa. This meant that the material of concrete structure and the tendons was still in the elastic stage during this pressurization period. In addition, the results of paper [16] showed the radial displacement of containment. The strain of tendon changed little and seemed to be proportional to pressure before the pressure reached 0.6 MPa. According to the works mentioned above, the material of concrete and tendons was still in the elastic stage if the inner pressure was under 0.585 MPa. As a result, the elastic material property was adopted to simplify the FEM model. The material properties of FEM model are listed in Table 1.

Table 1. Material properties of the finite element method (FEM) model.

Material	Elasticity Modulus (MPa)	Poisson Ratio	Density (kg/m³)	Thermal Expansion Coefficient
Concrete	3.45×10^4	0.2	2500	-
Steel liner	2.1×10^5	0.28	7850	-
Prestress tendon	1.9×10^5	-	7850	1.2×10^{-5}
Rebar	2×10^5	-	7850	-

The PCCV was prestressed by 223 horizontal, 144 vertical and 174 dome tendons with the nominal cross section area 2.85×10^{-3}, 5.4×10^{-3} and 2.85×10^{-3} m². In order to simulate the prestressing force, thermal expansion coefficient was adopted. Through temperature fall, the prestressing force was applied on every prestress tendon. The temperature fall magnitude was calculated by Equation (2).

$$\sigma = E \cdot \varepsilon = E \cdot \alpha \cdot \Delta T \tag{2}$$

σ is prestress force, E is elasticity modulus of tendon, ε is tendon strain, α is the thermal expansion coefficient, ΔT is temperature fall magnitude. The prestressing force of all the tendons was 1413 MPa.

Through Equation (2), the temperature fall magnitude ΔT was $-603.846\ ^\circ$C. Besides, six kinds of reinforcements in two directions were modeled on the inner, outer and middle of concrete cylindrical wall.

2.4.4. Mesh

The concrete wall was meshed by 26,172 hexahedral solid elements of a basic size of 2 m. The concrete wall thickness direction was divided into 10 fractions to provide enough nodes for coupling the tendon nodes with concrete nodes. The steel liner was meshed with 1632 shell elements of size 2 m. The steel liner and concrete wall were connected by fixed contacts. Prestress tendon and steel rebar were meshed by 172,834 linear elements of size 2 m. In addition, rebar and concrete were also connected by fixed contacts. In total, the FEM model had 277,371 nodes. The FEM model is shown in Figure 6.

| (**a**) | (**b**) | (**c**) |
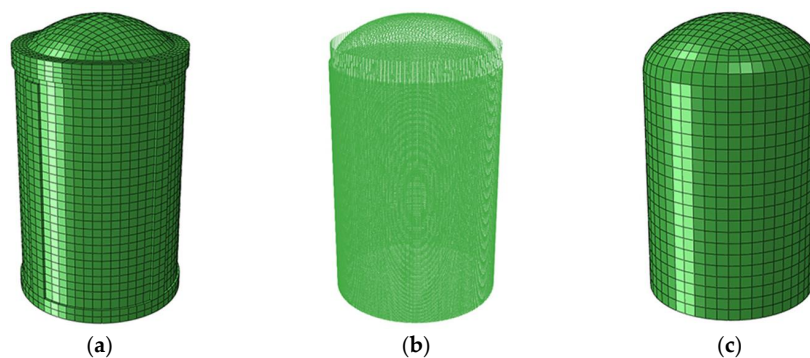
Figure 6. The FEM model. (**a**) Concrete; (**b**) Tendon and rebar; (**c**) Steel liner.

2.4.5. Load

Firstly, the model was constrained in six directions at the bottom of PCCV foundation slab. Secondly, self-weight was applied to the PCCV. Thirdly, prestress force was applied to all tendons. At last, inner pressure was applied on the steel liner to simulate ILRT. The pressure direction was perpendicular to the inner surface of steel liner. The load step history of inner pressure variation was in proportion to the real pressure time table as shown in Figure 4.

The load step history is listed in Table 2. In the calculation, it is assumed that the time unit is an hour. The inner pressure change time of 40 h is in proportion to the real time history of about 230 h.

Table 2. Load step history.

Load Step	Time (unit: h)
Gravity	20
Prestress	20
Inner pressure	40

3. Results

3.1. Monitoring Results

3.1.1. General Measure Points

After about 230 h of measurements, the data were processed with temperature compensating and then exchanged to strain [19]. The results from measuring point No. 1 (MP 1) to measuring point No. 4 (MP 4) are plotted in Figure 7. The vertical direction strain is shown by the red line while the circumferential direction strain is shown by the green line. In addition, pressure time table is a dashed

line in every picture. As can be seen from Figure 7, the height of pressure time table is set the same which indicates the pressure variation trend. The pressure value 0 MPa and 0.483 MPa is marked beside the pressure time table.
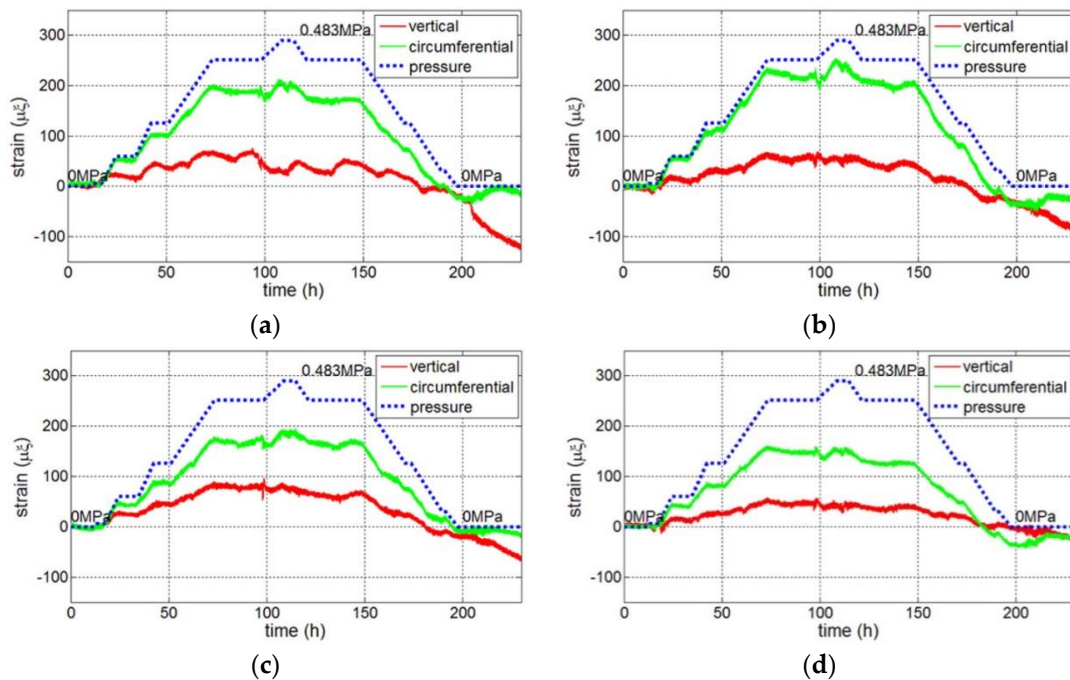
Figure 7. The monitoring results in vertical direction and circumferential direction. (**a**) Measuring point MP 1; (**b**) MP 2; (**c**) MP 3; (**d**) MP 4.

From Figure 7a–d, it is clear that the strain in two directions had the same trend compared with pressure variation. Using FBG to monitor PCCV is feasible. Take the results of MP 1 as an example. The strain maintained almost the same at 0 $\mu\varepsilon$ during the first 12 h, then the strain of cylindrical wall increased along with the pressure increase. At the time of pressure 0.483 MPa, the circumferential direction strain reached the maximum 200 $\mu\varepsilon$ whereas the vertical direction strain was about 40 $\mu\varepsilon$. This meant circumferential direction expansion was larger than the vertical direction expansion. After the highest pressure, the strain decreased along with the pressure decrease. However, there were many differences from MP 1 to MP 4 which might be caused by different location, concrete material property and so on.

There was a phenomenon that the measuring strain from 121 h to 148 h was 10 $\mu\varepsilon$ lower than the strain from 73 h to 98 h (see Figure 7a–d). However, the pressure was the same value, 0.42 MPa, during the two periods. Meanwhile, the temperature changed regularly on the order of 5 °C during the test. If the thermal expansion coefficient of concrete is 1×10^{-5}, 5 °C would cause 50 $\mu\varepsilon$ every day, which is visible in the vertical direction strain (see Figure 7a). The strain discrepancy between 73 and 98 h and 121 and 148 h may be caused by the temperature fluctuation. However, the temperature between these two periods seemed not very large, so there may be another reason explaining this phenomenon. The reason for this phenomenon might be that the FBG was fixed on the concrete wall by glue instead of a bolt. Although a bolted connection might be a better choice, a bolt was not used in order to protect the concrete surface. Obviously, glue creep might occur during the ILRT. As a consequence, the creep led to a tiny strain on each FBG.

During the last 30 h (200 h to 230 h), as shown in Figure 7a,d, the vertical direction strain decreased with value -30 $\mu\varepsilon$ and -100 $\mu\varepsilon$. Considering that the vertical direction strain changed about 50 $\mu\varepsilon$ at highest pressure, this decrease was very huge. The main cause of this phenomenon was concrete material thermal contraction. As mentioned before, α_h was not considered in Equation (1) for

simplification. Therefore, temperature compensation FBG could not compensate the thermal expansion of concrete. Fortunately, the thermal expansion or contraction strain of concrete material was relatively small when the temperature changed regularly.

In site, an abrupt temperature drop of about 11 °C happened at between 200 h and 230 h (see Figure 8). This phenomenon caused an abrupt strain decrease as shown in Figure 8a. During the first 200 h of monitoring, the temperature changed with a certain circulation. In general, the temperature decreased to the minimum value about 23 °C at night and increased to the maximum value of about 30 °C in daylight. However, at 200 h, temperature had a sudden drop about 11 °C. Because the concrete of the PCCV was sensitive to temperature change, it had a thermal contraction strain about -100 $\mu\varepsilon$ in the vertical direction.
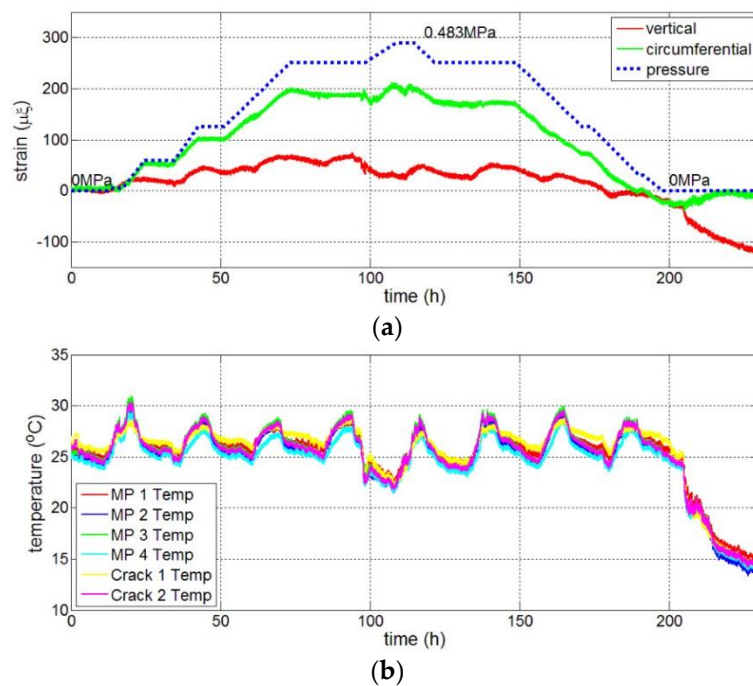
Figure 8. Comparison between the strain of MP 1 and measured temperature. (**a**) MP 1; (**b**) Temperature of each measure point.

That vertical direction strain was sensitive to an abrupt temperature drop while circumferential direction strain was not sensitive to temperature drop was an interesting phenomenon. One possible cause was that the prestressing in the circumferential and vertical directions was different. Due to the higher value of compression strain caused by the circumferential tendons which will be later discussed in the Section 3.2.1, the strain caused by temperature abrupt drop would have less effect on the circumferential direction strain. The real cause of this phenomenon needs further study.

3.1.2. Crack Measure Points

Apart from four general measurement points, the results of two crack measuring points are shown in Figure 9. The crack is shown in Figure 2b. In site, the crack was vertical so that two FBG sensors were horizontal with an upper one and a lower one in height. The strain of crack No. 1 seemed just like the general measuring points. However, the strain of crack No. 2 reached 330 $\mu\varepsilon$ which was the maximum of all FBGs. In contrast to other measuring points, during the time from 100 h to 123 h, the strain of crack No. 2 had a sharp increase of about 130 $\mu\varepsilon$ at 0.483 MPa compared to 0.42 MPa. As the pressure inside the PCCV increased, the compression strain in the circumferential direction decreased (see Figure 10). During this period, the prestress loss happened. In the actual engineering, the prestress was conducted to the concrete by the grouting in the prestress duct. However, the prestress was not

uniform so the crack started to open at the low prestress site. As shown in Figure 9, the strain of crack No. 2 was larger than for crack No. 1 at 0.42 MPa. This meant that the prestress loss at crack No. 2 was larger than that at crack No. 1. Now that the cracks had opened, this meant the prestress was overcome by the inner pressure. Without the prestress constraint, crack No. 2 had larger strain variation due to the prestress loss. It was possible that the strain of crack No. 2 continued to increase. As a result, the PCCV was not tight enough and the leakage might happen there due to increasing inner pressure. Therefore, crack No. 2 should be paid more attention.
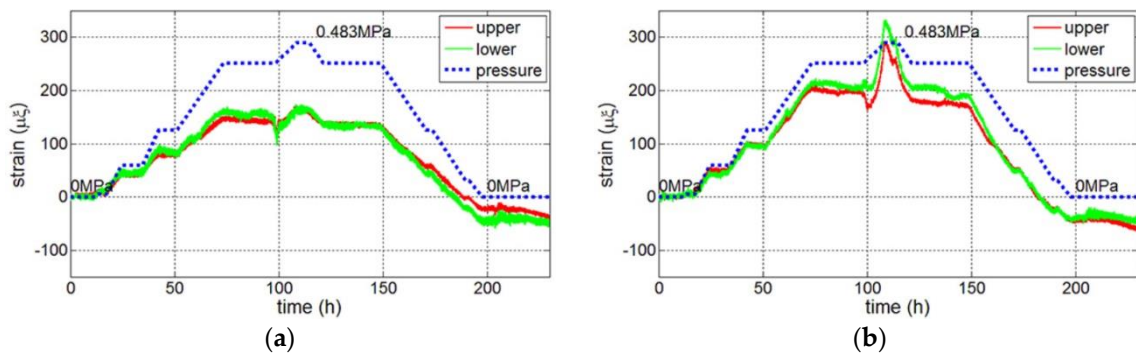
Figure 9. The strain of two crack measuring points. (**a**) Crack No. 1; (**b**) Crack No. 2.
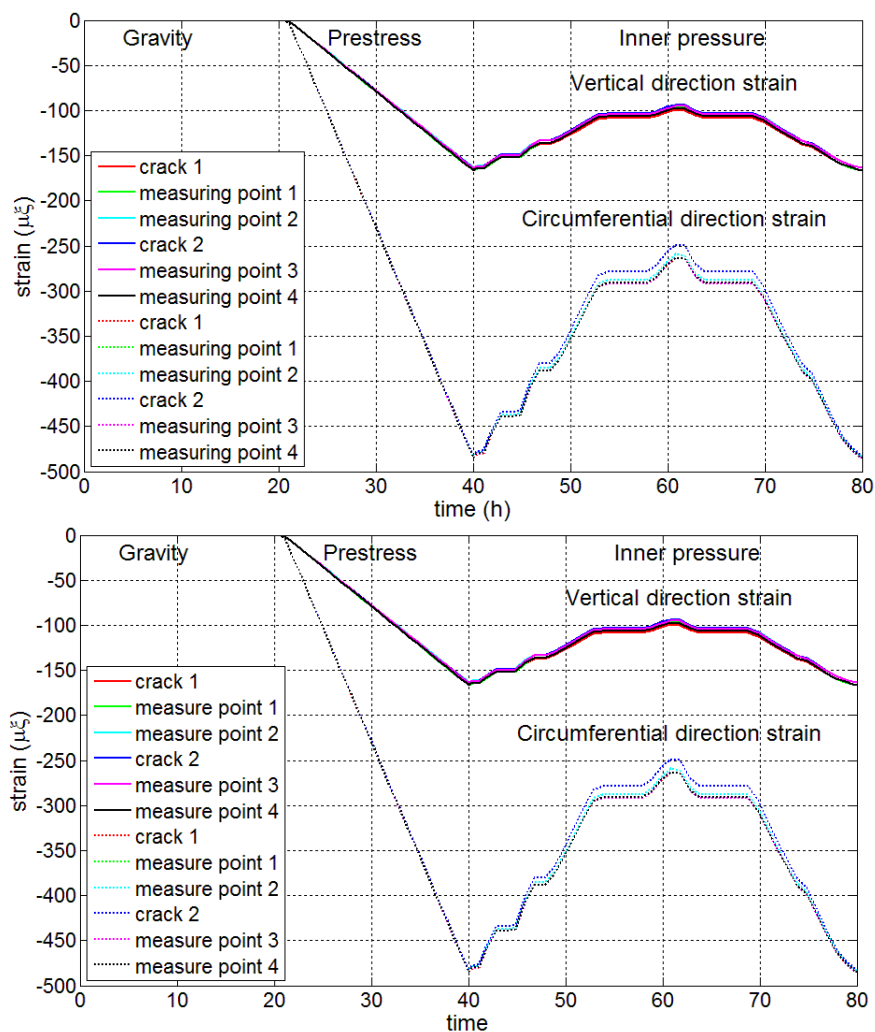
Figure 10. The results of vertical direction strain and circumferential direction strain.

3.2. The FEM Model Results

3.2.1. The Load Step History

In the FEM model, the elements 10,801, 10,426, 9426 and 14,401 were close to the measuring points from MP 1 to MP 4. Besides, element 10,076 and element 9451 were close to crack 1 and crack 2. Therefore, the results of the elements mentioned above were summarized. The strain of vertical and circumferential direction is shown in Figure 10. During the time from 0 to 20 h, the strain in two directions had little change. At the prestress load step (time from 20 to 40 h), the strain in two directions was compression strain with huge difference in magnitude. At the end time of prestress force, the vertical and circumferential direction strains were −482 and −166 με. At the time of maximum inner pressure, the vertical and circumferential direction strain came to −250 and −93 με. It was clear that the concrete cylindrical wall was still subjected to the compression strain at maximum inner pressure. This meant that there was no tension strain occurring at the concrete surface. The prestress tendons were still working to protect the concrete from cracking and the material was still elastic. Because the FEM model was ideal, especially in that the concrete material property difference was not considered, there was little difference between each measuring point.

3.2.2. The Strain Distribution

The principal object of this part was to find the regularities of strain distribution on the cylindrical wall. The strain in two directions was calculated and compared to the monitoring results. At the maximum inner pressure, the strain distribution in two directions is shown in Figure 11.
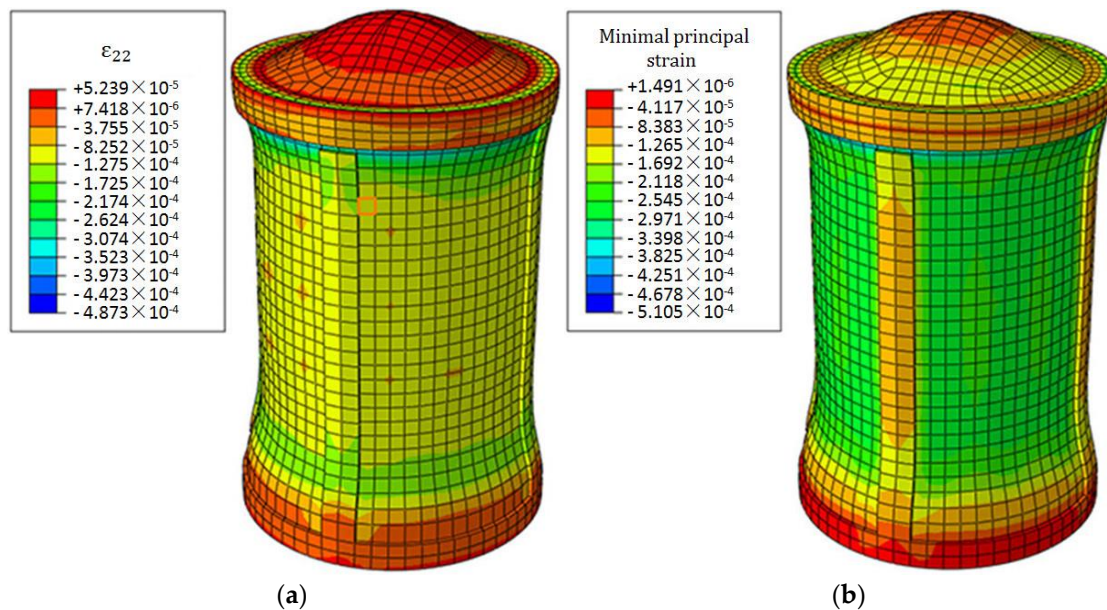
Figure 11. The strain distribution contour in two directions at the maximum inner pressure. (Deformation scale factor is 500.) (**a**) Vertical direction strain contour; (**b**) Circumferential direction strain contour.

The vertical strain on concrete surface is ε_{22} (Figure 11a). ε_{22} varied from 82 με to 127 με with elevation from +4 m to +40 m. The junction of the dome and cylinder which was near the ring girder had the maximum value. As the ring girder was the place where the vertical prestress tendons and dome tendons were anchored, this place might bear stress concentration. Besides, the minimum principal direction strain is the same as circumferential strain (see Figure 11b). The circumferential direction strain showed small difference from elevation 0 m to +45.8 m with magnitude from 211 με to 297 με. The maximum strain, about 382 με, also occurred at the junction of the dome and cylinder.

As a consequence, the strain in two directions was relatively high at the junction of the dome and cylinder. According to the strain distribution regularities, more FBG sensors should be installed at this place.

3.2.3. Comparison between Monitoring Results and Calculation Results

As mentioned previously, the concrete surface strain was compression strain from the calculation results (see Figure 10). In the engineering, the strain sensors could only measure the strain development after the installation time. As a result, the strain of time 40 h (see Figure 10) was set as a baseline. Then the calculation strain subtracted the baseline value during the ILRT. Obviously, the strain was positive after subtraction. In the FEM model, elements 10,801, 10,426, 9426 and 14,401 were close to measuring points 1 to 4. The results of these elements are plotted in Figure 12. In each direction, the strain discrepancy was small. The maximum discrepancy value is 12 $\mu\varepsilon$ in the circumferential direction at 0.483 MPa (Figure 12b).
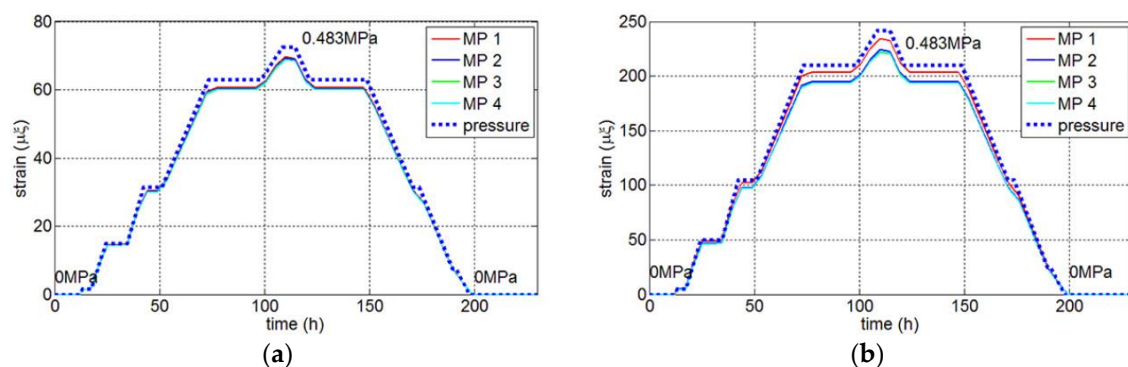
Figure 12. The calculation results in two directions. (**a**) Vertical direction strain; (**b**) Circumferential direction strain.

In order to testify the calculation results, the comparison between monitoring results and calculation results was made (Figure 13). Because there was little difference between the calculation results of four measuring points, the calculation results of MP 4 were chosen as a representation. The monitoring results and calculation results were plotted in Figure 13.

It turned out that the calculation results were consistent with monitoring results of four measuring points during the first 110 h. However, the discrepancy became larger and larger after 110 h. During the time from 200 h to 230 h, the decrease rate of monitoring results became faster, mainly due to the abrupt temperature drop (see Figure 8b). The huge discrepancy was caused by temperature change. In the future, temperature change simulation should be done for more precise simulation.

Compared to vertical direction strain, circumferential direction strain was not sensitive to abrupt temperature drop during 200 h to 230 h (see Figure 13b). The calculation results showed good consistence with monitoring results.

Figure 14 shows the concrete strain-inner pressure relationship. Comparing the calculation results with monitoring results, it was clear that both monitoring results and calculation results showed a similar trend. During the pressurization process, the monitoring results kept almost linear growth until 0.4 MPa. When it came to 0.45 MPa and 0.483 MPa, the monitoring results even decreased while the calculation results were still linear. The calculation results maintained almost the average value of the monitoring results of four measuring points during pressurization. During the depressurization process, the monitoring results were almost below the calculation results. This phenomenon might be caused by glue relaxing of FBGs.

(**a**)

(**b**)
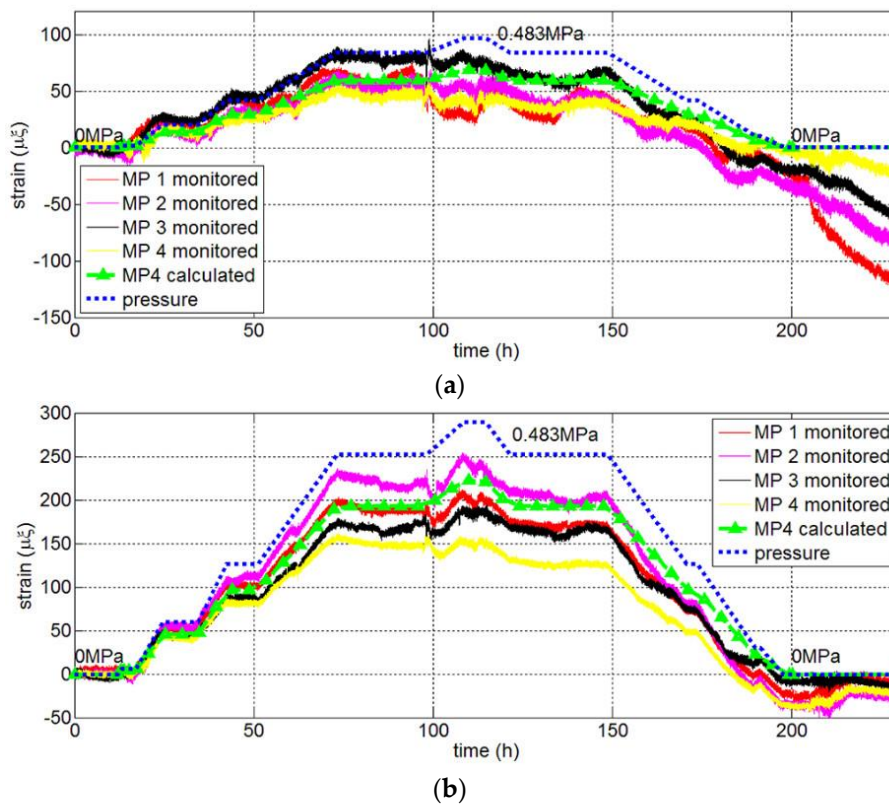
Figure 13. The comparison between monitoring results and calculation results. (**a**) Vertical direction; (**b**) Circumferential direction.

(**a**)

(**b**)

(**c**)

(**d**)
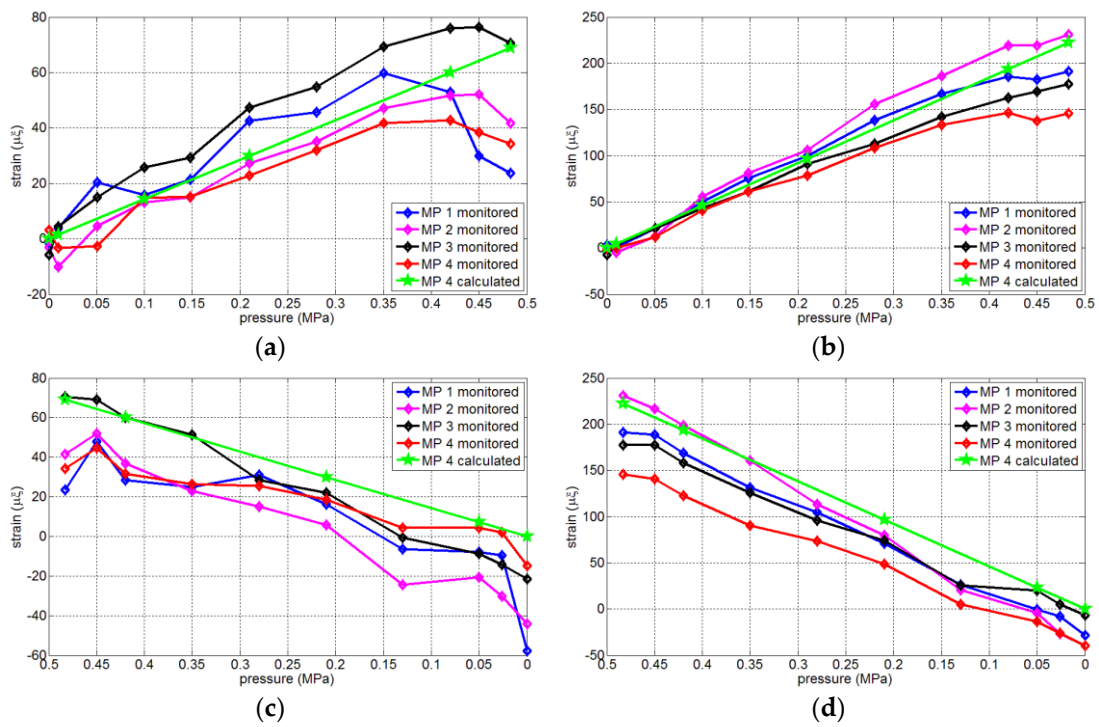
Figure 14. Concrete strain-inner pressure relationship. (**a**) Vertical direction during pressurization; (**b**) Circumferential direction during pressurization; (**c**) Vertical direction during depressurization; (**d**) Circumferential direction during depressurization.

Then, on comparing the vertical direction monitoring results with circumferential direction, it seemed that there were more fluctuations in vertical direction monitoring results. In order to verify this conclusion, linear regression was used in data fitting of each measuring point because the trend of monitoring results was almost linear. At the same time, the ratio of residual sum of squares (RSS) to total sum of squares (SYY) [20] could be calculated as shown in Table 3. The smaller the ratio is, the more accurate the linear regression will be and fewer fluctuations will exist. From Table 3, it can be concluded that the circumferential monitoring results had fewer fluctuations both in the pressurization process and depressurization process.

Table 3. The ratio of residual sum of squares (RSS) to total sum of squares (SYY).

Phase	Measure Point	Vertical	Circumferential
pressurization	MP 1	0.5372	0.0193
pressurization	MP 2	0.0785	0.0106
pressurization	MP 3	0.0516	0.0071
pressurization	MP 4	0.1244	0.0324
depressurization	MP 1	0.2718	0.0033
depressurization	MP 2	0.0388	0.0026
depressurization	MP 3	0.0083	0.011
depressurization	MP 4	0.0954	0.0046

The reason of this phenomenon should be discussed. Because the maximum values of vertical direction and circumferential direction were 50 με to 70 με and 150 με to 240 με respectively, the external disturbance especially temperature change of concrete material would have greater effect on vertical direction monitoring results. As a result, there were fewer fluctuations in circumferential direction.

Apart from these, the ratios listed in Table 3 were relatively small. This meant the concrete strain–inner pressure relationship was almost linear. That is, the material of PCCV was still in the elastic stage. Therefore, the material elastic hypothesis of FEM model mentioned above was proven.

4. Conclusions

In this paper, the PCCV monitoring project by using FBG sensors provided us much information about the PCCV structure during the ILRT and showed good potential. Because the monitoring results of each strain FBG had the same trend compared with pressure variation, the feasibility of FBG had been proven. The results showed FBG could be widely used in PCCV structure health monitoring. During the data process stage, the FBG strain caused by temperature change could be eliminated by temperature-compensating FBG. However, the strain caused by concrete thermal expansion or contraction could not be eliminated by using temperature-compensating FBG. According to the monitoring results, the vertical direction strain changed about −100 με due to the abrupt temperature drop of 11 °C. Nevertheless, the circumferential direction strain was not sensitive to abrupt temperature drop compared to vertical direction strain.

The monitoring results of each measuring points indicated that the circumferential direction strain was higher than vertical direction strain during ILRT. However, strain magnitude differences existed between four measuring points. This might be caused by the direction and the concrete material property.

There were two cracks monitored by four FBGs. The results showed that crack No. 1 had the same trend compared with general measuring points while crack No. 2 had a sudden increase about 130 με at 0.483 MPa. Attention should be paid to the sudden increase of crack No. 2 to prevent further cracking.

In addition, a FEM model was built to simulate the ILRT process. Because the maximum inner pressure was 0.483 MPa and this magnitude was far from the ultimate inner pressure, the elastic

material property was chosen for simplification. The calculation load step history in proportion to real ILRT time was imposed on the FEM model. The results showed that there was little difference on the strain magnitude of each direction due to the homogeneous material property. Besides, the calculation results were very close to the monitoring results, so the calculation results were proven. In addition, the strain distribution contour in two directions could give advice about where strain sensors should be installed. According to the results, more FBGs should be installed at the junction of the dome and cylinder. Moreover, the concrete strain–inner pressure relationship was compared between monitoring results and calculation results. Apparently, the relationship was almost linear. There were more fluctuations in the vertical direction monitoring results which might be caused by temperature change. Because the concrete strain–inner pressure relationship was almost linear, the material elastic hypothesis of FEM model mentioned above was proven.

Author Contributions: Xuefeng Zhao, Kaixing Liao, Changsen Sun, Xianglong Kong and Jinke Li conceived and designed the experiments; Xuefeng Zhao, Kaixing Liao, Changsen Sun, Xianglong Kong, Jinke Li, Shengyuan Li and Xinwang Zhang performed the experiments and collected the monitoring data; Jinke Li, Xuefeng Zhao, Kaixing Liao and Xianglong Kong analyzed the data; Jinke Li built the FEM model; Jinke Li and Xuefeng Zhao wrote the paper.

Conflicts of Interest: The authors declare no conflict of interest.

References

1. Glišić, B.; Simon, N. Monitoring of concrete at very early age using stiff SOFO sensor. *Cem. Concr. Compos.* **2000**, *22*, 115–119. [CrossRef]

2. Hessheimer, M.F.; Shibata, S.; Costello, J.F. Functional and Structural Failure Mode Overpressurization Tests of 1: 4-Scale Prestressed Concrete Containment Vessel Model. In Proceedings of the 17th International Conference on Structural Mechanics in Reactor Technology (SMiRT 17), Prague, Czech Republic, 17–22 August 2003; H02-3.

3. Zhao, X.; Cui, Y.; Wei, H.; Kong, X.; Zhang, P.; Sun, C. Research on corrosion detection for steel reinforced concrete structures using the fiber optical white light interferometer sensing technique. *Smart Mater. Struct.* **2013**, *22*, 1693. [CrossRef]

4. Inaudi, D.; Glisic, B. Long-Range Pipeline Monitoring by Distributed Fiber Optic Sensing. *J. Press. Vessel Technol.* **2010**, *132*, 763–772. [CrossRef]

5. Ferdinand, P.; Magne, S.; Marty, V.; Georges, T. Optical fibre Bragg grating sensors for structure monitoring within the nuclear power plants. *Proc SPIE* **1994**, *2425*, 11–20.

6. Jang, J.B.; Hwang, K.M.; Lee, H.P.; Kim, B.H. An assessment of the prestress force on the bonded tendon by SI and impact signal analysis techniques. *Nucl. Eng. Des.* **2013**, *255*, 9–15. [CrossRef]

7. Leng, J.; Asundi, A. Structural health monitoring of smart composite materials by using EFPI and FBG sensors. *Sens. Actuators A Phys.* **2003**, *103*, 330–340. [CrossRef]

8. Wan, C.; Hong, W.; Liu, J.; Wu, Z.; Xu, Z.; Li, S. Bridge Assessment and Health Monitoring with Distributed Long-Gauge FBG Sensors. *Int. J. Distrib. Sens. Netw.* **2013**, *2013*, 494260. [CrossRef]

9. Perry, M.; Yan, Z.; Sun, Z.; Zhang, L.; Niewczas, P.; Johnston, M. High stress monitoring of prestressing tendons in nuclear concrete vessels using fibre-optic sensors. *Nucl. Eng. Des.* **2014**, *268*, 35–40. [CrossRef]

10. Li, W.; Ho, S.; Song, G. Corrosion Detection of Steel Reinforced Concrete Using Combined Carbon Fiber and Fiber Bragg Grating Active Thermal Probe. *Smart Mater. Struct.* **2016**, *25*. Available online: http://iopscience.iop.org/article/10.1088/0964-1726/25/4/045017/meta (accessed on 14 March 2016).

11. Hu, H.; Lin, Y. Ultimate analysis of PWR prestressed concrete containment subjected to internal pressure. *Int. J. Press. Vessel. Pip.* **2006**, *83*, 161–167. [CrossRef]

12. Sang, H.N.; Moon, I.H.; Lee, J.B.; Kim, J.H. Analysis of Prestressed Concrete Containment Vessel (PCCV) under Severe Accident Loading. *Nucl. Eng. Technol.* **2008**, *40*, 77–86.

13. Lee, H.P. Shell finite element of reinforced concrete for internal pressure analysis of nuclear containment building. *Nucl. Eng. Des.* **2011**, *241*, 515–525. [CrossRef]

14. Bílý, P.; Kohoutková, A. Sensitivity analysis of numerical model of prestressed concrete containment. *Nucl. Eng. Des.* **2015**, *295*, 204–214. [CrossRef]

15. Jones, C.A.; Dameron, R.; Sircar, M. Improving the state of the art in FEM analysis of PCCVs with bonded and unbonded prestress tendons. *Nucl. Eng. Des.* **2015**, *295*, 782–788. [CrossRef]

16. Shokoohfar, A.; Rahai, A. Nonlinear analysis of pre-stressed concrete containment vessel (PCCV) using the damage plasticity model. *Nucl. Eng. Des.* **2016**, *298*, 41–50. [CrossRef]

17. Hill, K.O.; Meltz, G. Fiber Bragg grating technology fundamentals and overview. *J. Lightwave Technol.* **1997**, *15*, 1263–1276. [CrossRef]

18. Pereira, G.; McGugan, M.; Mikkelsen, L.P. Method for independent strain and temperature measurement in polymeric tensile test specimen using embedded FBG sensors. *Polym. Test.* **2016**, *50*, 125–134. [CrossRef]

19. Jung, D.W.; Kwon, I.B.; Choi, N.S. Application of a Temperature-Compensating FBG Sensor to Strain Measurement. *Adv. Mater. Res.* **2007**, *26–28*, 1089–1092. [CrossRef]

20. Weisberg, S. *Applied Linear Regression*; John Wiley & Sons: Hoboken, NJ, USA, 2005; pp. 35–36.